



# Preparation, Characterization and Photocatalytic Properties of Visible-Light-Driven CuO/SnO<sub>2</sub>/TiO<sub>2</sub> Photocatalyst

M. Golestanbagh<sup>1</sup> · M. Parvini<sup>1</sup> · A. Pendashteh<sup>2,3</sup>

Received: 12 February 2018 / Accepted: 5 April 2018 / Published online: 11 May 2018  
© Springer Science+Business Media, LLC, part of Springer Nature 2018

## Abstract

Shifting the ultra-violet of titania to visible light driven photocatalysis can be realized by coupling with metallic or non-metallic elements. In this study, a highly efficient visible-light-responsive SnO<sub>2</sub>/CuO/TiO<sub>2</sub> heterojunction were synthesized via sol-gel method followed by calcination at different temperatures. The crystalline structures, morphology, constituent contents, chemical state and optical properties of the samples were analyzed in detail. The photodegradation performances of the prepared samples were evaluated by studying the degradation of 2,4-dichlorophenol under UV and visible light irradiation. Among the series of synthesized nanocomposites, the one prepared using Sn(Cu)/Ti molar ratio of 0.1 (SC10) was found to be the most active photocatalyst for the degradation of organic pollutants under investigation. This remarkably improved photocatalytic activity of SC10 could be attributed to the strong absorption of visible light and effective separation of photoinduced e<sup>-</sup>-h<sup>+</sup> pair. The mineralization of 2,4-dichlorophenol was investigated by HPLC/MS and IC analysis. The recycling experiments confirm that SnO<sub>2</sub>/CuO/TiO<sub>2</sub> nanocomposite is essentially stable. The work may set foundation for application of the new photocatalyst of CuO/SnO<sub>2</sub>/TiO<sub>2</sub> and make an important step forward remedying environmental pollution.

---

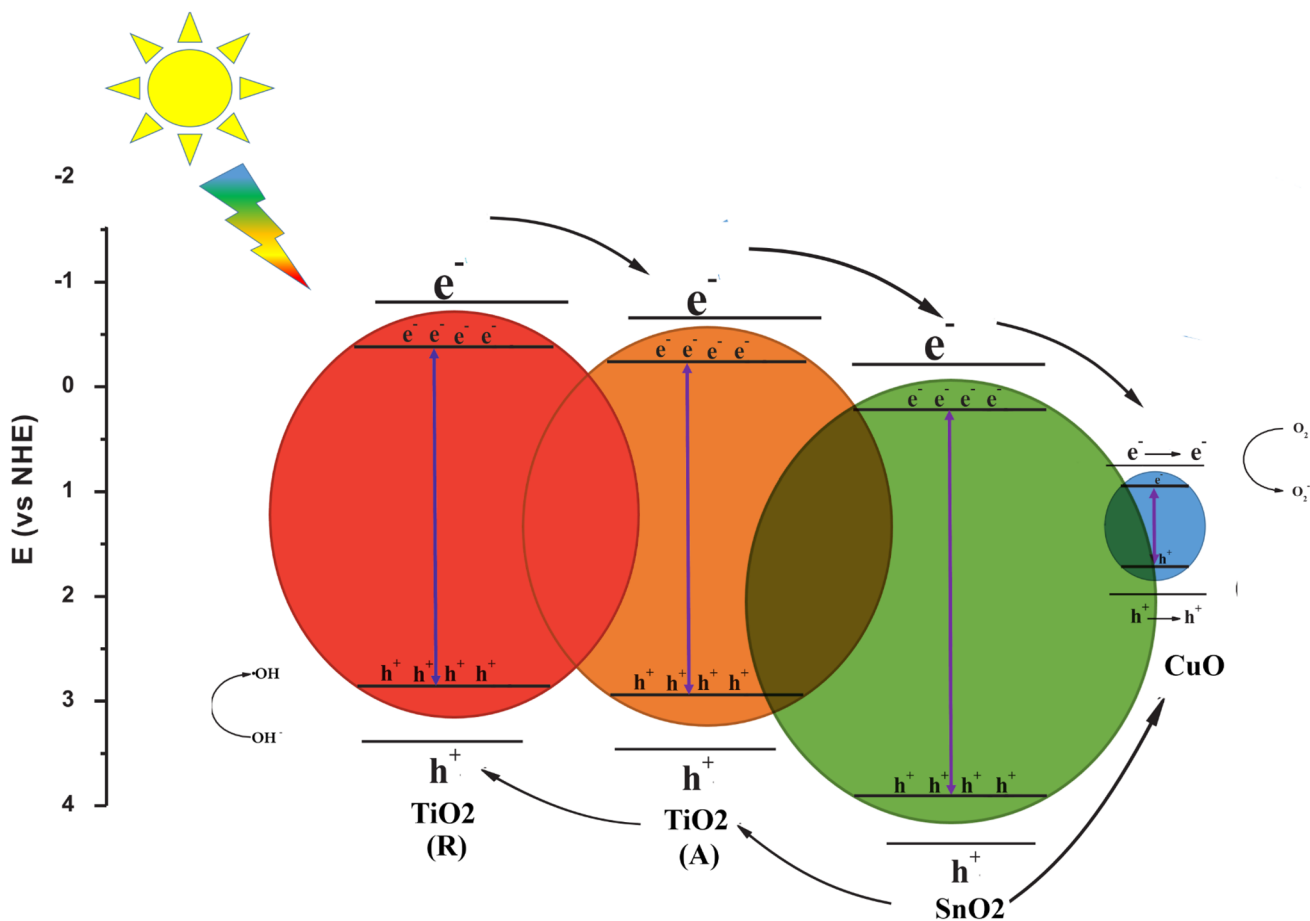
✉ M. Parvini  
m.parvini@semnan.ac.ir

<sup>1</sup> Faculty of Chemical, Petroleum and Gas Engineering,  
Semnan University, Semnan, Iran

<sup>2</sup> Environmental Science Department, Faculty of Natural  
Resources, University of Guilan, Rasht, Iran

<sup>3</sup> The Caspian Sea basin Research Center, University  
of Guilan, Rasht, Iran

## Graphical Abstract



**Keywords** Photocatalyst · Visible light · Nanocomposite ·  $\text{TiO}_2$  · Sol-gel

## 1 Introduction

Photocatalysis has attracted a great deal of attention as a promising candidate for the elimination of organic contaminants in water and air, since the pioneering work by Honda and Fujishima [1]. The photocatalytic reaction is caused by the use of ultraviolet (UV) radiation to stimulate the semiconductor materials [2]. During irradiation of semiconductor photocatalysts with UV, photons are absorbed by the semiconductors and electron ( $e^-$ )–hole ( $h^+$ ) pairs are generated [3, 4]. However, these photocatalysts show low efficiency under the sun light because UV constitutes only 3% of the total solar energy [5]. From the perspective of both chemistry and practical applications, it is undoubtedly important to develop photocatalytic materials that harvest photons with wider wavelength range [6]. Various strategies have been proposed to efficiently separate the photogenerated electron–hole pairs in semiconductor photocatalysts, for instance by doping, metal loading, and/or

introducing heterojunctions. A heterojunction, in general, is defined as the interface between two different semiconductors with unequal band structure, which can result in band alignments. Among the proposed strategies, engineering heterojunctions in photocatalysts has been proved to be one of the most promising ways for the preparation of advanced photocatalysts because of its feasibility and effectiveness for enhancing the optical adsorption of photocatalyst [5, 7]. It also can efficiently reduce the recombination rate of the photogenerated charge carriers in the use of environmental purification and remediation [8].

$\text{TiO}_2$  [9],  $\text{SnO}_2$  [10, 11] and  $\text{CuO}$  [5], as three well-known semiconductors, have been intensively investigated in the fields of photocatalysis, solar cell and gas sensors due to their special electronic and optical properties. Titanium dioxide ( $\text{TiO}_2$ ) has and continues to be one of the most widely studied semiconductors for photocatalytic applications due to its advantages, such as a suitable band gap for redox reactions, long-term stability, low cost, nontoxicity

and so on [12]. However, as a single component semiconductor photocatalyst,  $\text{TiO}_2$  has an inherent drawback that the photogenerated electron/hole ( $e^-/h^+$ ) pairs recombine fast ( $\sim 10$  ns) and hence only a fraction of  $e^-/h^+$  pairs are available for the photoreaction [13]. To date, this disadvantage can be overcome by means of semiconductor coupling. With this approach, the assembled semiconductors are selected suitably so that efficient charge transfer occurs between them [14, 15]. This condition spatially separates the photoexcited electrons and holes onto the different constituents and reduces the rate of  $e^-/h^+$  pair recombination.

In multi-heterostructure, the presence of different facets exhibit distinct abilities in modifying the interfaces for better interaction [16]. Several studies on ternary composites such as  $\text{CdS}/\text{TiO}_2/\text{WO}_3$ ,  $\text{TiO}_2$ -based  $\text{V}_2\text{O}_5/\text{WO}_3$ ,  $\text{Au}/\text{TiO}_2/\text{WO}_3$ ,  $\text{CuO}/\text{SnO}_2/\text{TiO}_2$ ,  $\text{SnO}_2/\text{TiO}_2/\text{WO}_3$ ,  $\text{Cu}_2\text{O}/\text{TiO}_2/\text{g-C}_3\text{N}_4$ ,  $\text{ZnS}/\text{ZnO}/\text{CNT}$ ,  $\text{Fe}_3\text{O}_4/\text{ZnO}/\text{CuWO}_4$  and  $\text{Cu}/\text{Cu}_2\text{O}/\text{CuO}$  had shown good photoelectric performance [5, 8, 17–25]. The couplings of  $\text{TiO}_2$  with  $\text{CuO}$  or  $\text{SnO}_2$  have been reviewed to greatly enhance the photocatalytic activities in photocatalytic activity by the spatial charge separation efficiency [26–33]. The position of conduction band of  $\text{SnO}_2$  and  $\text{CuO}$  that is lower than  $\text{TiO}_2$  is perfect for the occurrence of charge transfer which reduces the recombination of electron–hole. The presence of  $\text{CuO}$  with low band gap (1.7 eV) on submonolayer of  $\text{TiO}_2$  surface not only leads to visible light absorption but also increases the surface acidity for the absorption of more hydroxyl ion and organic reactants [34, 35]. Conversely,  $\text{SnO}_2$  with wide band gap of 3.9 eV has no absorption of light at wavelength longer than 330 nm. However, when coupled with  $\text{TiO}_2$ , its photocatalytic activity enhance under visible light [36, 37]. It is reported that this system can considerably improve the photocatalytic activity of  $\text{TiO}_2$ , which is attributed to the enhancement of the charge carrier separation due to the different energy band gap position of  $\text{TiO}_2$  and  $\text{SnO}_2$ , leading to the formation of a cascaded structure [38]. On the basis of the discussion above, the mixed oxides of two semiconductors (e.g.  $\text{CuO}/\text{TiO}_2$  and  $\text{SnO}_2/\text{TiO}_2$ ) as coupling system have attracted extensive interests, and the catalyst samples have been also intensely produced by a variety of synthetic routes [20, 21, 25–28, 31, 32, 34, 35, 37, 38].

On the basis of above discussion, up to date very few studies have been carried out on trimetallic oxide composites. To further make the most of the advantages and hedge the shortcomings of the abovementioned three semiconductors, herein, we designed and synthesized a novel  $\text{CuO}/\text{SnO}_2/\text{TiO}_2$  ternary heterostructure nanohybrid, displaying an excellent visible-light photocatalytic activity. We presume that mixed oxides of  $\text{TiO}_2$ ,  $\text{CuO}$  and  $\text{SnO}_2$  with different energy gap would lead to the formation of cascaded structure that would enhance the activity. The photocatalyst were characterized by X-ray diffraction (XRD),

scanning electron microscopy (SEM), energy dispersive X-ray (EDX) analysis, transmission electron microscopy (TEM), Raman spectroscopy, ultraviolet–visible diffuse reflectance spectroscopy (UV–vis-DRS), and X-ray photoelectron spectroscopy (XPS). To evaluate the catalytic activity of the synthesized materials, photodegradation experiments were also conducted with 2,4-dichlorophenol (2,4-DCP) under visible light. 2,4-DCP was selected because it is considered a representative compound of an important family of priority pollutants in aquatic environments [39–42]. Importantly, the initial photocatalytic degradation mechanism of 2,4-DCP was elucidated by means of a gas chromatography–mass spectrometry (GC–MS) study of the degradation intermediates. The mechanism of improved photocatalytic activity for  $\text{SnO}_2/\text{CuO}/\text{TiO}_2$  was probed using photoluminescence spectroscopy. Our findings suggest that incorporation of  $\text{SnO}_2$  and  $\text{CuO}$  into  $\text{TiO}_2$  as a complex system can extend the spectral response to the visible region and that the photocatalytic activity is greatly enhanced due to the promotion of the electron transfer through the interfacial potential gradient in the hybrid structure.

## 2 Materials and Methods

### 2.1 Materials

All chemicals were used as received without further purification. Titanium tetraisopropoxide (TTIP, 99.99%) and copper(II) sulfate pentahydrate ( $\text{CuSO}_4 \cdot 5\text{H}_2\text{O}$ , 99.99% purity) were purchased from Sigma-Aldrich, Tin(IV) chloride pentahydrate ( $\text{SnCl}_2 \cdot 5\text{H}_2\text{O}$ ), Ethanol and 2,4-DCP were from Merck.

### 2.2 Preparation of $\text{CuO}/\text{SnO}_2/\text{TiO}_2$ Composite Photocatalyst

Sol–gel was adopted to synthesize  $\text{CuO}/\text{SnO}_2/\text{TiO}_2$  composite system in the present work. In brief, 0.02 mol TTIP were added dropwise into 50 ml absolute ethanol to give a solution which was then vigorously stirred for 30 min at room temperature. The desired amounts of  $\text{SnCl}_2 \cdot 5\text{H}_2\text{O}$  and  $\text{CuSO}_4 \cdot 5\text{H}_2\text{O}$  (the molar ratio of Sn–Cu was 1:1) were then added in the reaction mixture while stirring continuously for 80 min until the Sn and Cu dopant dissolved. An amount of 2 ml of deionized water was then dropped into the above solution. Afterwards, the resultant solution mixture was maintained at room temperature with continuous stirring for 24 h to form a gel which was then aged for 12 h at room temperature. The samples were dried at 80 °C overnight and then annealed at 450, 550 and 650 °C for 4 h. The resultant composite materials coupled with different Cu and Sn contents by adjusting the molar ratio of Sn(Cu) to Ti from

0.05 to 0.20 were named as SC5, SC10, SC15 and SC20, respectively. Different composites composition were listed in Table 1.

### 2.3 Material Characterization

X-ray diffraction (XRD) analysis was performed using Bruker AXS D5000 diffractometer utilizing Cu K $\alpha$  radiation ( $\lambda = 1.5406 \text{ \AA}$ , 40 kV, 30 mA) at  $0.050^\circ$  intervals with 1 s count accumulation per step. The data was collected in the region of  $2\theta = 20^\circ\text{--}80^\circ$ . Diffuse reflectance UV–vis (DRUV) spectra were recorded using a PerkinElmer Lambda 35 spectrophotometer, with BaSO<sub>4</sub> used as reference. Photoluminescence (PL) emission spectra of the samples were measured using FLSP920 Edinburgh with 450 W xenon lamp. The morphology of the samples were analysed using FESEM (SU8020, Hitachi) equipped with an energy dispersive Xray spectrometer (EDX, INCA/350, Oxford). Transmission electron microscopy (TEM) images were obtained with JEOL TEM 2100 high-resolution (HR) TEM (200 kV). The X-ray photoelectron spectroscopy (XPS) measurements were carried out using a PerkinElmer RBD upgraded PHI-5000C ESCA system with monochromatic Mg K excitation and a charge neutralizer. All bonding energies were calibrated to the C 1s peak at 284.8 eV of the surface adventitious carbon.

### 2.4 Evaluation of Photocatalytic Activity

The photocatalytic activity of all photocatalysts were determined by the photodegradation for 2,4-DCP solution (pH = 5.35) under vis irradiation ( $k > 400 \text{ nm}$ ). A sunlamp (Philips HPA 400/30S, Belgium) was used directly for the UV photocatalytic reaction, while for the visible photocatalysis a cutoff filter ( $k > 400 \text{ nm}$ ) was employed to remove UV irradiation. The photocatalyst dosages were 30 mg for visible photocatalysis and 10 mg for UV photocatalysis, respectively, which were suspended in 2,4-DCP solution. The reactor was perpendicular to the light beam and located 10 cm away from the light source. The intensity of the UV light and visible light on the samples is evaluated to be 0.2 and 0.1 W/cm<sup>2</sup>, respectively. An electric fan is applied to cool down the photocatalytic reactor. The suspension was magnetic stirred at  $(25 \pm 2)^\circ\text{C}$  in the dark for 30 min to

reach adsorption equilibrium before irradiation, and oxygen gas was continuously bubbled through the solution at a flux of  $1 \text{ ml min}^{-1}$ . The concentration change of 2,4-DCP was monitored by measuring the UV/vis absorption spectra of the suspension at regular 30 min intervals, using a Shimadzu UV/vis 2550 spectrophotometer. Owing to the very small particle size of CuO/SnO<sub>2</sub>/TiO<sub>2</sub>, for each measurement the suspension was filtered three times using a filter syringe to remove the insoluble photocatalyst before UV/vis measurements. GC–MS analysis of the intermediates formed during the mineralisation of 2,4-DCP was obtained using a Shimadzu GC–MS 2010 equipped with a silica capillary column by injecting  $\sim 0.1 \mu\text{l}$  of a 500 ppm initial concentration of 2,4-DCP in water. The reproducibility of the photocatalytic degradation was evaluated by repeating experiments at least three times with different batches of photocatalysts prepared by the same procedure.

## 3 Results and Discussion

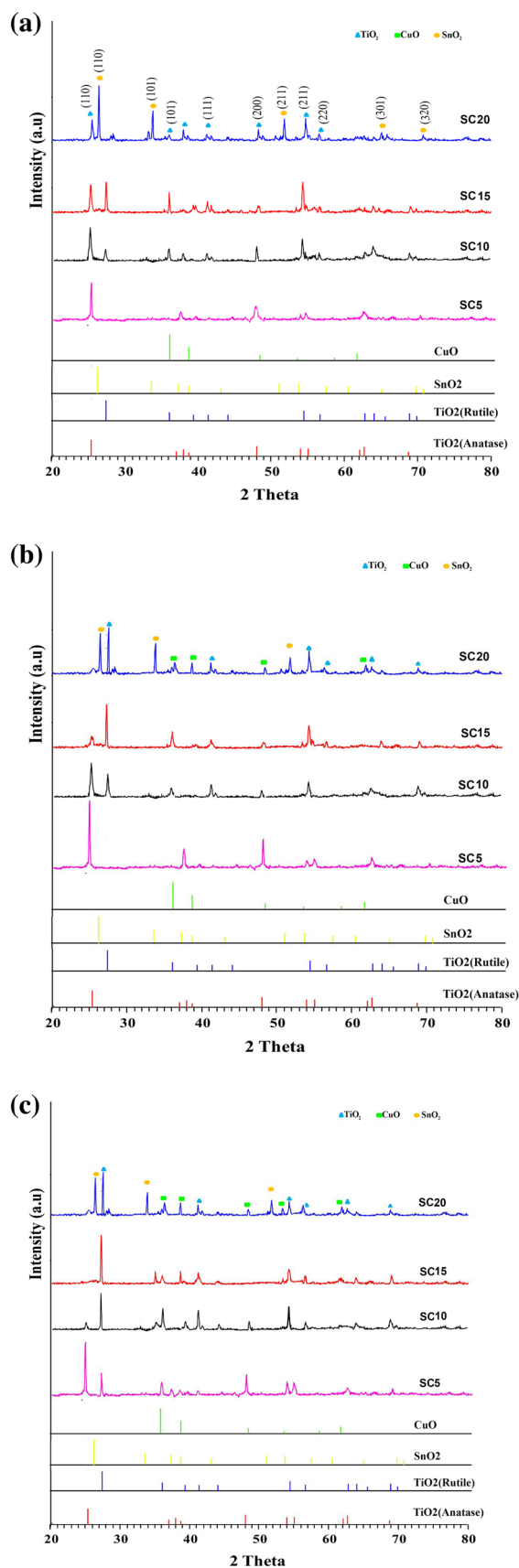
### 3.1 The X-ray Diffraction (XRD)

The X-ray diffraction (XRD) patterns for CuO/SnO<sub>2</sub>/TiO<sub>2</sub> calcined at different temperatures are depicted in Fig. 1. The calcinations temperatures were 450, 550 and 650 °C, respectively. It can be seen from Fig. 2a that the composite photocatalyst annealed at 450 °C exhibit pure anatase structure of TiO<sub>2</sub> at low Sn and Cu doping level (SC5), no other phases were detected in the SC5 heterojunctions. With the increase of the metal cations doping level, the SC10 mainly has anatase structure, with a minor content of rutile structure. Further increasing the Sn(Cu) doping content, the main (1 1 0) Bragg peak of rutile is observed to become sharper and more intense, indicating that the formation of a large amount of rutile structure in the SnO<sub>2</sub>/CuO/TiO<sub>2</sub> composite catalyst. Moreover, a strong diffraction peak at around  $26.6^\circ$  was observed in the XRD patterns of SC20 sample indicating the presence of a small amount of rutile SnO<sub>2</sub> [31].

Figure 1b shows the XRD data of CuO/SnO<sub>2</sub>/TiO<sub>2</sub> composite semiconductors annealed at 550 °C. It can be observed that the SC5 sample has anatase as the dominant phase, and the main structure of SC10 sample is still anatase structure, while a weak peak appears at around  $27.2^\circ$ , indicating the formation of a small amount of rutile phase [37]. Compared with SC10, the SC15 sample heated at 550 °C shows a main rutile structure, with some anatase peaks remaining. Whereas, a pure rutile phase is observed in SC20 sample, suggesting that the phase transition from anatase to rutile in the sample occurs. Besides the diffraction peaks for anatase and rutile TiO<sub>2</sub>, there are two new crystalline structures (rutile SnO<sub>2</sub> and CuO, respectively) formed in SC20 sample after annealing, which may be explained by that the

**Table 1** Different composites composition

Sample	TiO <sub>2</sub> (%)	SnO <sub>2</sub> (%)	CuO (%)
SC5	95	2.5	2.5
SC10	90	5	5
SC15	85	7.5	7.5
SC20	80	10	10



◀ **Fig. 1** XRD patterns of the synthesized composites at different Sn (Cu) ratio and calcination temperature **a** 450 °C **b** 550 °C **c** 650 °C

tin and copper atomic content have reached saturation in the lattice at higher doping level [43].

The XRD spectra of  $\text{CuO}/\text{SnO}_2/\text{TiO}_2$  composite semiconductors annealed at 650 °C shows that the significant structure change occurs compared with those of the composite photocatalyst annealed at 450 and 550 °C. As can be seen from Fig. 1c, the SC5 sample shows a mixture of anatase and rutile phase, in addition to the impurity peaks corresponding to CuO that are also present in the composite  $\text{CuO}/\text{SnO}_2/\text{TiO}_2$  sample. With the increase of tin and copper doping level, the diffraction peaks corresponding to anatase  $\text{TiO}_2$  disappeared and only rutile  $\text{TiO}_2$  as well as CuO phase was observed for the SC15 sample, implying the anatase structure is completely transformed into rutile phase. Interestingly, it was also observed the significant diffraction peaks of rutile phase  $\text{SnO}_2$  in the XRD spectra of the SC20 sample except for the  $\text{TiO}_2$  and CuO structure. On the basis of the above analysis, it could be found that the Sn and Cu ions doped in  $\text{TiO}_2$  can promote the phase change from anatase to rutile  $\text{TiO}_2$  in the range of annealing temperature from 450 to 650 °C. Moreover, higher annealing temperature (650 °C) not only leads to the formation of the impurity such as CuO, but also favors the growth of rutile structure and gives  $\text{CuO}/\text{SnO}_2/\text{TiO}_2$  catalysts with larger particle size (Table 2). Thus, a fine control of calcination temperature is crucial for obtaining a pure  $\text{CuO}/\text{SnO}_2/\text{TiO}_2$  heterostructure.

### 3.2 Raman Spectra

Figure 2 shows the Raman spectra of  $\text{CuO}/\text{SnO}_2/\text{TiO}_2$  catalysts synthesized by sol-gel methodology, and the obtained samples were calcined at 550 °C. Here, it can be seen that

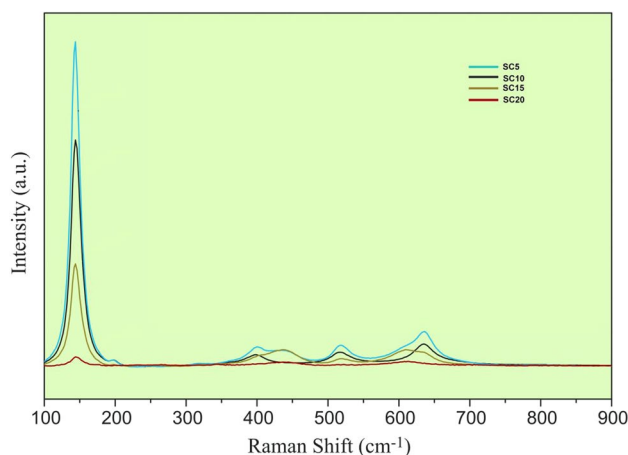


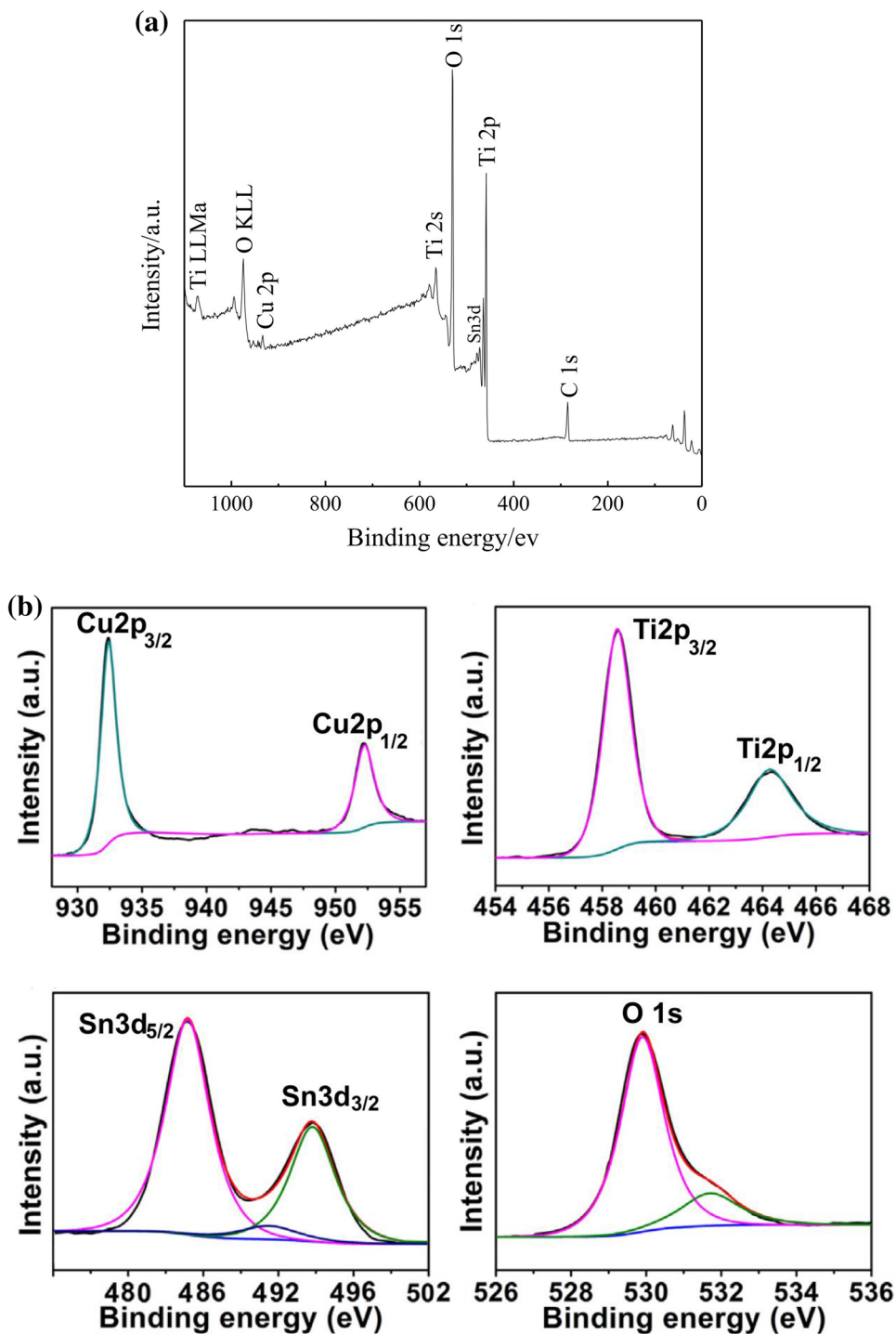
**Fig. 2** Raman spectra of composite with different Sn(Cu) ratio

all Raman spectra of composite catalyst samples exhibit rather similar spectra, four well-defined bands at 144, 399, 514 and 639  $\text{cm}^{-1}$  were observed, which are characteristics of anatase structure [44]. Interestingly, as the Sn(Cu) dopant content increases, the intensity of main Raman band at 144  $\text{cm}^{-1}$  assigned to anatase  $\text{TiO}_2$  gradually reduced, indicating a lower crystallinity and small amount of anatase  $\text{TiO}_2$  for the composite photocatalysts [45].

### 3.3 X-ray photoelectron Spectroscopy

Further verification on the nature of surface defects and chemical state of the metal oxides was carried out using XPS that is known for its surface sensitive analysis. Figure 3 shows the typical XPS results of SC15 catalyst annealed at 550  $^{\circ}\text{C}$ . As can be seen from Fig. 3a, the X-ray photoelectron spectroscopy survey spectrum indicates that the

**Fig. 3** X-ray photoelectron spectroscopy for SC15 **a** wide scan, **b** Cu 2p, Ti 2p, Sn 3d and O 1s





SC15 sample contains predominantly O, Ti, Sn, Cu and C elements. It is thought to be the residual carbon from the organic precursor solution and the adventitious carbon from the XPS instrument itself are the main reason to cause the presence of C element.

The XPS spectra of Cu 2p region was shown in Fig. 3b. The figure shows the appearance of the two signals at 938.4 (Cu 2p<sub>3/2</sub>) and 958.9 eV (Cu 2p<sub>1/2</sub>); these signals demonstrate the presence of Cu<sup>2+</sup> in CuO [46]. The difference in the binding energy gap value between the Cu 2p<sub>3/2</sub> and Cu 2p<sub>1/2</sub> is 20.5 eV, which confirms the presence of CuO [5, 34, 35, 47]. On the other hand, the shake-up peaks indicate the presence of an unfilled Cu 3d<sub>9</sub> shell and reconfirm the presence of Cu<sup>2+</sup> in the tested composite [48], which coincide with the Cu<sup>2+</sup> position with oxygen. It is known that the radius of Cu<sup>2+</sup> is 0.73 Å, which is larger than that of Ti<sup>4+</sup> [46]. Thus, the Cu<sup>2+</sup> ion is not able to replace the Ti<sup>4+</sup> site and occupy its position in theory during the preparation. It is therefore thought that the Cu<sup>2+</sup> ions possibly resided over the surface of TiO<sub>2</sub> particle [46]. In Fig. 3b, the Ti 2p XPS spectra of SC15 has two peaks centered at 458.5 and 463.9 eV, which are attributed to the Ti 2p<sub>3/2</sub> and 2p<sub>1/2</sub> spin–orbital splitting photoelectrons in Ti<sup>4+</sup>. These data agree well with previously reported XPS data for TiO<sub>2</sub> [46]. Additionally, the band located at the low binding energy (458.5 eV) is broad and asymmetric, demonstrating that there are at least two kinds of Ti chemical states. The peak identified at 457.4 eV suggests the existence of Ti<sup>3+</sup> in the composite catalyst [49, 50], and the formation of Ti<sup>3+</sup> shows the presence of lots of oxygen vacancies during the doping process. Figure 3b shows the Sn 3d XPS spectra of SC15. The binding energy of 485.6 and 494.6 eV is ascribed to Sn 3d<sub>5/2</sub> and Sn 3d<sub>3/2</sub>, respectively, assigned to Sn in 4+ state species [51]. According to the literature [52], the peak position corresponding to Sn 3d<sub>3/2</sub> is centered between those of Sn 3d<sub>3/2</sub> (485.0 eV) in metallic Sn and Sn 3d<sub>3/2</sub> in SnO<sub>2</sub> (486.6 eV), which suggests the Sn<sup>4+</sup> ions incorporated into lattice of TiO<sub>2</sub> and caused a small structural distortion in SC15 sample. Besides, it is worthy to be noted that the peak at 499.0 eV is due to a plasmon peak (P) in clean Sn metal [53]. The O 1s XPS spectrum is shown in Fig. 3b, too. It can be observed that the broad peak of O 1s is asymmetric, and that can be fitted by two peaks at 528.8 and 530.1 eV, indicating there are two independent chemical states for O within SC15. The peak located at high binding energy for O element can be corresponded to surface hydroxyl groups such as Ti–OH and Ti–O–O [21].

### 3.4 UV–vis Diffuse Reflectance Spectra

The results of UV–vis diffuse reflectance spectra of the catalysts calcined at 550 °C are shown in Fig. 4. The absorption edges for all the samples fall in the visible region

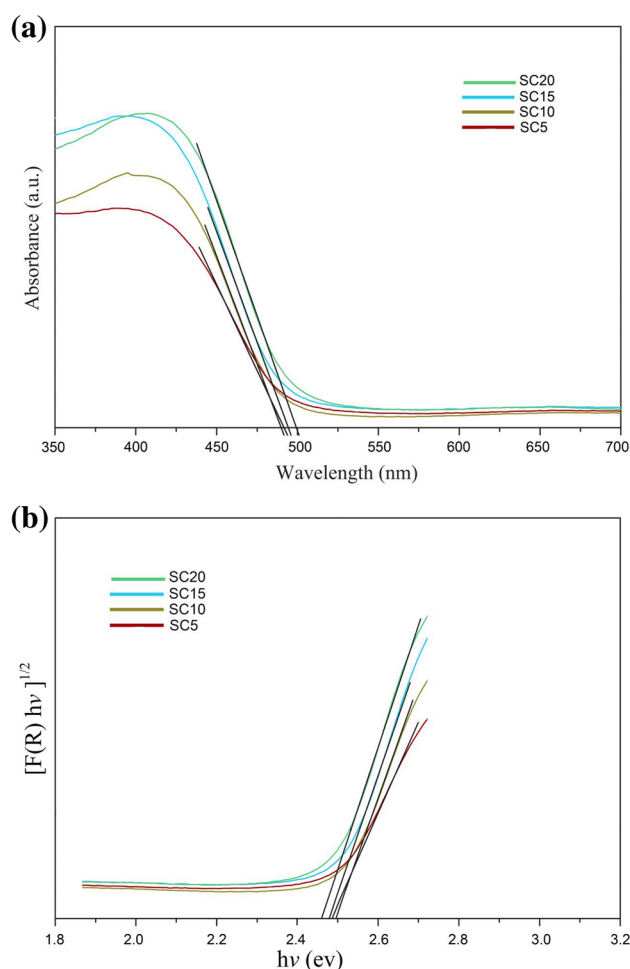


**Fig. 4** **a** Absorption spectra and **b** band gap determination for SnO<sub>2</sub>/CuO/TiO<sub>2</sub> calcined at 550 °C

( $k > 400$  nm) which indicates that the entire sample is active at visible light. The optical absorption edges of SnO<sub>2</sub>/CuO/TiO<sub>2</sub> samples locate in the range of 480–500 nm, corresponding to a band gap energy ( $E_g$ ) of approximately 2.41–2.31 eV. It also can be seen that the band gap decreases monotonically with increasing Sn and Cu concentration, implying that the level of Sn and Cu co-doping has a remarkable effect on the optical absorption of CuO/SnO<sub>2</sub>/TiO<sub>2</sub> composite catalysts.

### 3.5 Photoluminescence (PL) Spectroscopy

To further address the contribution of charge transfer in the suppression of the recombination of electron hole process which is vital in the photocatalytic reaction [40], photoluminescence (PL) spectroscopy was investigated. Figure 5 shows the photoluminescence spectra attained for all the photocatalysts which were almost identical in shape and position.

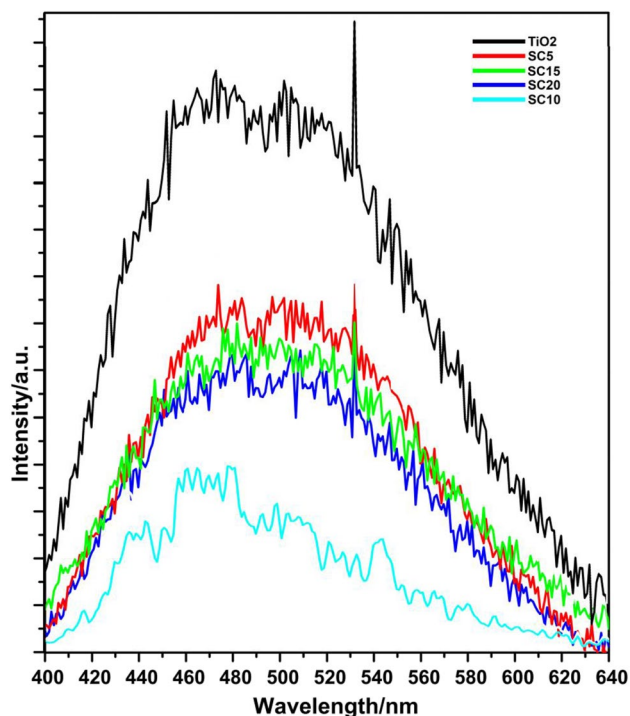


**Fig. 5** Photoluminescence spectra of nanocomposite calcined at 550 °C

The two peaks at around 480 and 520 nm in all samples could be ascribed to the transition from oxygen vacancies with one trapped electron and two trapped electrons to the valence band of  $\text{TiO}_2$ , respectively [2]. Pure  $\text{TiO}_2$  exhibits a highest PL intensity. The PL intensity is further weakened when  $\text{CuO}$  and  $\text{SnO}_2$  were incorporated indicating that the recombination of photoinduced charge carriers is inhibited. This confirms that heterojunction is formed at the interface between  $\text{TiO}_2$ ,  $\text{SnO}_2$  and  $\text{CuO}$ . Photo-induced electrons would be shifted from the higher CB of  $\text{TiO}_2$ - $\text{SnO}_2$  and  $\text{CuO}$ . Moreover, as the VB potential of  $\text{CuO}$  is above than  $\text{SnO}_2$ , this might lead to hole transfer in multiple pathways. The holes from the lower valence band of  $\text{SnO}_2$  would be transferred to  $\text{TiO}_2$  and  $\text{CuO}$ . Subsequently, the holes from  $\text{TiO}_2$  would move to  $\text{CuO}$  thus promoting the separation of electron-hole pairs. The emission intensity of SC10 that is lower than SC15 and SC20 signifies a lower recombination rate of hetero-generated electrons and holes. This could be correlated to the higher amount of oxygen vacancies that exist in SC10 resulting in a decreased PL intensity. Therefore, SC10 photocatalyst with suppressed electron-hole recombination rate is expected to increase the photocatalytic reaction.

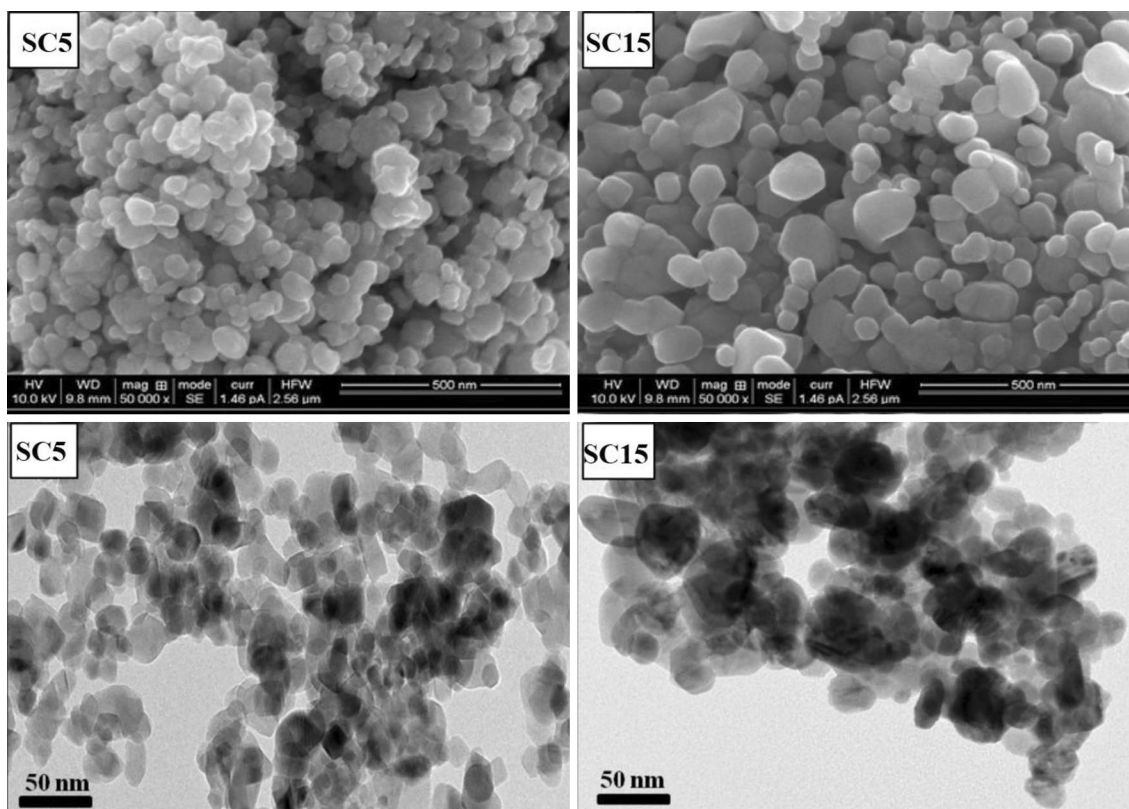


**Fig. 6** SEM/TEM images of nanocomposites calcined at 550 °C



### 3.6 SEM and TEM

Morphologies of the samples were characterized using SEM and TEM. Figure 6 clearly points out that all the samples (SC5 and SC15) are uniform. Increasing the amount of Sn(Cu) (Fig. 5b) caused the formation of denser particles and the agglomeration between them. These agglomerates were shaped by nanoparticles with an average size at around 30–70 nm. These values were consistent with the calculations made from the corresponding XRD patterns and Scherrer equation. Furthermore, the distribution of Sn(Cu) nanoparticles seemed to be randomly distributed on the TiO<sub>2</sub> nanoparticles. The EDX analysis was also employed to detect the chemical compositions of the CuO/SnO<sub>2</sub>/TiO<sub>2</sub> composite catalysts. Table 3 lists the chemical compositions and concentration of CuO/SnO<sub>2</sub>/TiO<sub>2</sub> samples with different Sn(Cu) content. The results of EDX analysis clearly reveal that the SC15 mainly composed of Ti, O, C, Cu and Sn, indicating that the as-prepared composite catalyst have the well-mixed heterojunctions, consistent with XPS and XRD finding. However, Cu element was not observed in the SC5 sample. This is probably due to the Cu content is quite low and dispersed unevenly on CuO/SnO<sub>2</sub>/TiO<sub>2</sub> when the Cu doping level is 0.05.

### 3.7 Photocatalytic Activity

To determine the efficiency of the photocatalysts, photocatalytic activity of nanocomposite was first investigated by evaluating the degradation of 2,4-DCP under UV light radiation. The catalyst adsorption capacity was tested before irradiation as seen in Fig. 7. Both composites and TiO<sub>2</sub> (Commercial) showed very good 2,4-DCP adsorption in the dark (around 10–20%). The adsorption was instantaneous and did

**Table 2** Characterisation of TiO<sub>2</sub>/SnO<sub>2</sub>/CuO composites

Samples	Calcinations temperature (°C)	Crystalline size (nm)			
		Anatase	Rutile	SnO <sub>2</sub>	CuO
SC5	450	16.2			
SC5	550	20.7			
SC5	650	21.2	27.2		4.5
SC10	450	11.1	6.1		
SC10	550	9.95	14.8		
SC10	650	13.6	17.9	11.3	6.3
SC15	450	11.3	7.21		
SC15	550	9.61	7.6	9.8	6.6
SC15	650	15.2		10.2	6.9
SC20	450	n.d. <sup>a</sup>		n.d. <sup>a</sup>	6.5
SC20	550	n.d. <sup>a</sup>		n.d. <sup>a</sup>	7.6
SC20	650	n.d. <sup>a</sup>		n.d. <sup>a</sup>	8.2

<sup>a</sup>Not determined due to the overlapping peaks ascribed to SnO<sub>2</sub> and rutile TiO<sub>2</sub>

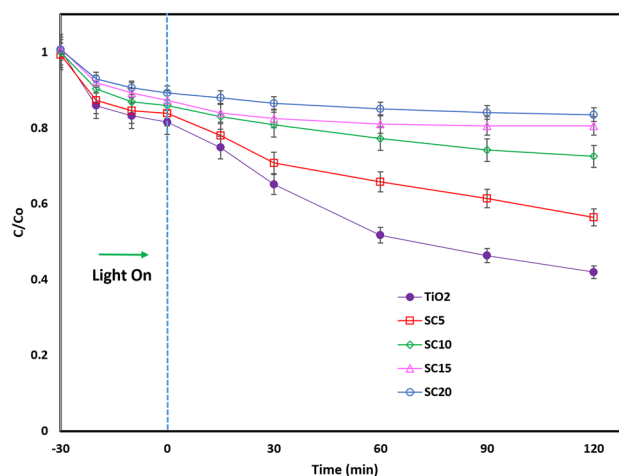


**Fig. 7** Photocatalytic activities composites calcined at 550 °C on photodegradation of 2,4-DCP under UV light irradiation with the photocatalyst dosage of 1.0 g/l and 2,4-DCP concentration of 20 mg/l

not increase with time. After 30 min, the light was turned on starting the photocatalytic process. As can be seen, the highest conversion of 2,4-DCP under UV LEDs was obtained with the TiO<sub>2</sub> and SC5 photocatalysts, while that of the other composites was slightly lower. Nonetheless the SC5 photocatalyst presented a quite similar 2,4-DCP conversion than that of TiO<sub>2</sub>, which could be attributed to a part of 2,4-DCP adsorbed on the composites, especially on the TiO<sub>2</sub> surface. This suggests that the only participant in the photocatalytic reaction under UV irradiation was TiO<sub>2</sub>; while deposited CuO and SnO<sub>2</sub> plays a negative role reducing the contact between the TiO<sub>2</sub> surface and the photons causing a reduction of 2,4-DCP degradation. This evidences that SnO<sub>2</sub> and CuO act like an impurity and the electron–hole pairs

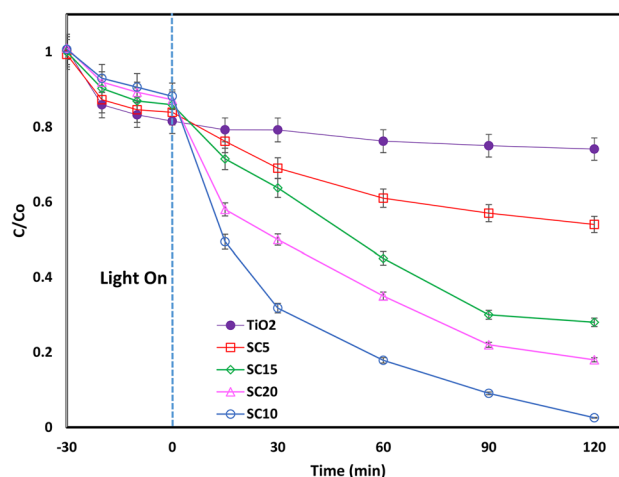


**Fig. 8** Photocatalytic activities composites calcined at 550 on photodegradation of 2,4-DCP under visible light irradiation with the photocatalyst dosage of 1.0 g/l and 2,4-DCP concentration of 20 mg/l

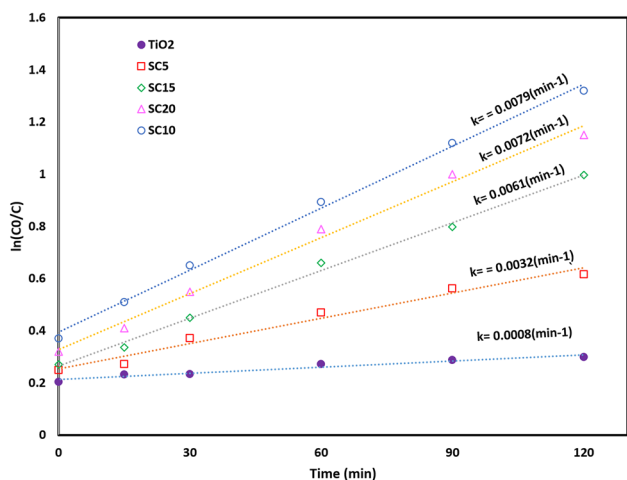


**Fig. 9** Kinetic curves composites on photodegradation of 2,4-DCP under visible light

generated by nanocomposite are rapidly recombined. When the photocatalytic process is carried on under visible light (470 nm), all of the composites showed a better 2,4-DCP

**Fig. 10 a** UV-vis absorption spectra during the 2,4-DCP photocatalytic, and **b** variation of 2,4-DCP and TOC concentrations and dechlorination rate during the 2,4-DCP photocatalytic degradation under visible light irradiation with the SC10 photocatalyst dosage of 1.0 g/l and 2,4-DCP concentration of 20 mg/l

degradation (Fig. 8). The enhanced photocatalytic activity of the composites at visible light could be associated with several synergetic effects as the presence of different facets on the photocatalysts and charge transfer at the interface. Reactive or high-energy facets on photocatalyst contribute significantly to their excellent activities in catalytic reactions. The adsorption of the molecules is intrinsically determined by surface atomic structures (facets) and the high surface acidity of CuO particles. The divergence in the energy levels drives the electrons and holes to different crystal faces. This suppressed the photoinduced electron-hole pair recombination which is the key to the high efficiency of the photocatalytic reaction [54]. It can also be seen that the co-doping level affects the photocatalytic activity, with the SC10 sample displaying the highest photocatalytic activity under visible light irradiation.

The photodegradation process of 2,4-DCP over the SnO<sub>2</sub>/CuO/TiO<sub>2</sub> composites is described as below:

$$\ln(c/c_0) = -kt \tag{1}$$

where  $C_0$  is the 2,4-DCP concentration before irradiation,  $C$  represents the 2,4-DCP concentration at reaction time  $t$ ,

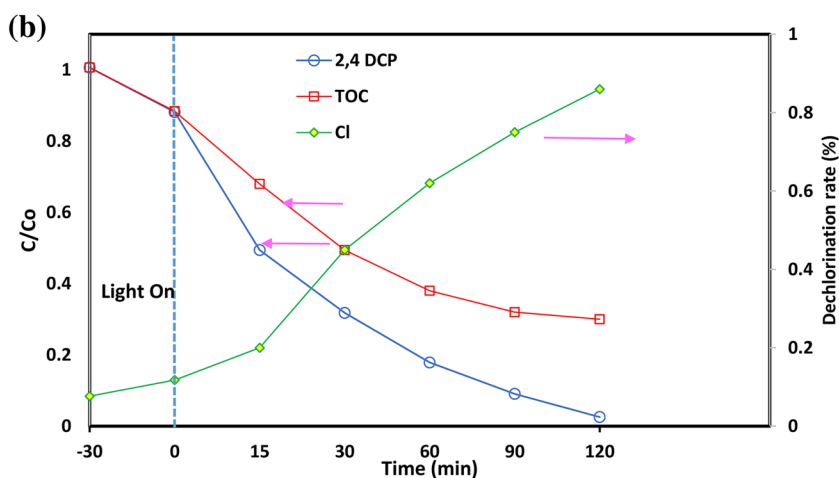
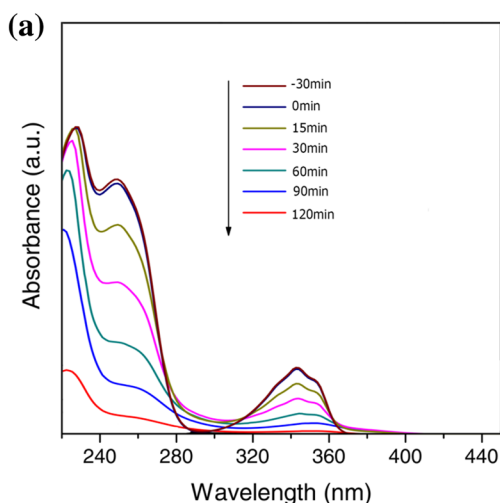
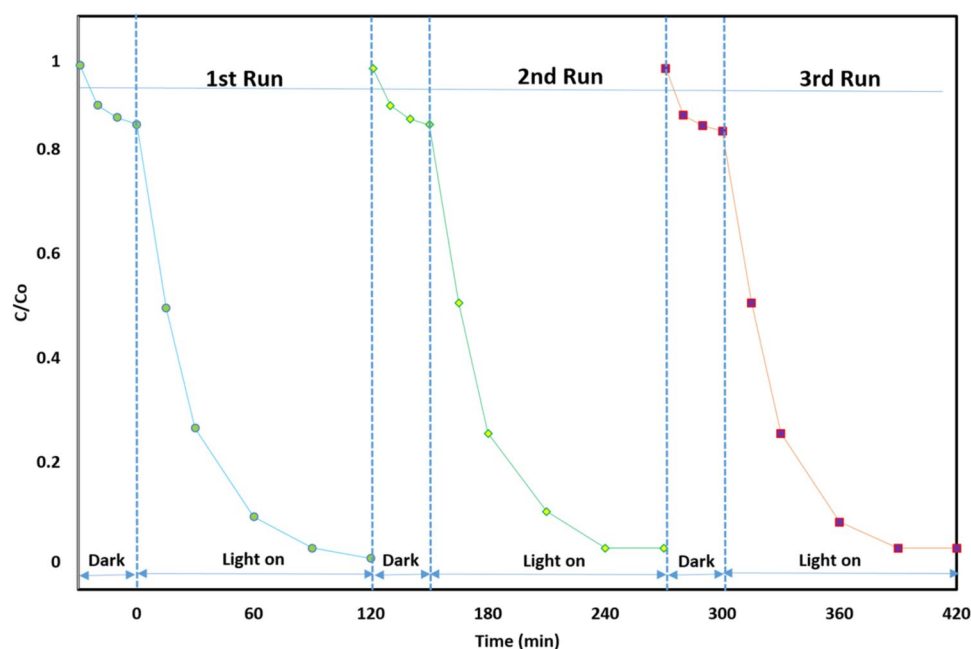


**Fig. 11** Cycling runs in photocatalytic degradation of 2,4-DCP in the presence of SC10 composite for 30 min in dark and following 120 min under visible light irradiation



and  $k$  is the pseudo-first-order rate constant. Figure 9 shows that the addition of Sn(Cu) to the composite promotes effectively the photocatalytic degradation of 2,4-DCP, and the SC10 composite exhibits highest photocatalytic efficiency ( $k=0.0079 \text{ min}^{-1}$ ).

Figure 10a shows that the intensity of the maximum absorption band at 352 nm reduce with an increase in irradiation time. As shown in Fig. 10b, the dechlorination rate of 2,4-DCP is 98% after 120 min irradiation, suggesting that the decomposition of 2,4-DCP mainly proceeds a chlorine-released pathway. Furthermore, the TOC removal rate of 2,4-DCP is 70% after 120 min irradiation under visible light (Fig. 10b). The repeated experiments of 2,4-DCP degradation is carried out to evaluate the stability of the SC10 composite (Fig. 11). The photocatalytic activity of the SC10 composite has no obvious variation during three photodegradation cycles, suggesting that the photocatalyst possesses high stability.

An attempt was made to identify the intermediate products formed during the irradiation process through mass spectrometry analysis. The sample was withdrawn from the reaction mixture at the time interval of 30 min and this aqueous sample was extracted into chloroform solvent. It can be seen from the mass spectra in Fig. 12 that the amount of 2,4-DCP decreased gradually as the irradiation time increased. It can be concluded from Fig. 12a–d that 2,4-DCP was decomposed into other new substances whose relative molecular masses were 128.21, 144, 126.2, 110.1, 108.2 and 60 respectively. Figure 12d shows that there were few of 2,4-DCP in the solution after 120 min of treatment. It indicated that most of 2,4-DCP were decomposed into other substances. According to the

**Table 3** EDX analysis of SC5 and SC15 in different positions

Sample	O (wt%)	C (wt%)	Ti (wt%)	Cu (wt%)	Sn (wt%)
SC-0.05 spectrum 1	53.21	4.68	36.86	–	5.25
SC-0.05 spectrum 2	44.62	2.23	45.59	–	7.56
SC-0.15 spectrum 1	35.39	2.88	35.73	9.1	16.9
SC-0.15 spectrum 2	50.21	2.29	28.91	7.73	10.86

relative molecular masses of intermediates and principles of organic degradation, the possible molecular structures of the intermediates were listed in Table 4. The intermediate products Chlorophenols, Hydroquinone, benzoquinone, Phenol were identified at 30 min irradiated sample. The Chlorohydroquinones, Hydroxybenzoquinone and Acetic acids were identified at 60 min irradiated sample. In chlorophenols, the attack of hydroxyl radical to the para position leads to the formation of hydroquinone. It undergoes oxidation and reduction to form benzoquinone. The degradation products chlorophenols are obtained by the addition of a hydroxyl radical to the position of the hydroxyl group of chlorophenols. The chlorohydroquinone is converted into hydroxyhydroquinone by oxidation with another hydroxyl radical followed by Cl abstraction. The hydroxybenzoquinone is formed either by the oxidation followed by reduction of hydroxyhydroquinone and the hydroxyl radical attack of benzoquinone. An attack of hydroxyl radicals on hydroxybenzoquinone and benzoquinone lead to the ring opening to form acetic acid. In addition, the

**Fig. 12** GC-MS spectrum of the photo-degraded products of 2,4 DCP ► at different irradiation time

degradation product chlorophenols is obtained by the addition of a hydroxyl radical to the position of the Cl of chlorophenols. The chlorophenols is converted into phenol by oxidation with another hydroxyl radical followed by Cl abstraction. The aliphatic compound, acetic acid is further oxidized into the smaller molecular weight aliphatic compounds and finally mineralized into CO<sub>2</sub> and H<sub>2</sub>O.

The research of Quanfang Lu showed that part of 2,4-DCP were decomposed into CO<sub>2</sub> and H<sub>2</sub>O by using glow discharge electrolysis [55]. The study of Ying Wang indicated that 2-chlorophenol and 4-chlorophenol may be the intermediate of the degradation of 2,4-DCP [56]. The study of Liu showed that 1,4-dihydroxybenzene was also an intermediate product of the degradation of 2,4-DCP [57]. Xu's research suggested that there were acetic acid and formic acid generated during the process of Fenton-like degradation of 2,4-DCP when Fe<sub>3</sub>O<sub>4</sub> magnetic nanoparticles as catalyst [58]. The study of Zhang showed that oxalic acid was a kind of degradation products of 2,4-DCP by using pulsed high voltage discharge [59]. Chung et al. showed that 2,4-DCP yielded less-chlorinated products, such as monochlorophenol and monochlorohydroquinone, and the non-chlorinated product, hydroquinone, which might have further reacted by photooxidation [60]. Devi and Nithya reported that the major identified intermediates are hydroquinone and benzoquinone [61]. Rakibuddin and Ananthkrishnan showed that after 5 h irradiation of 2,4-dichlorophenol by graphene encapsulated zn/co3o4 core-shell hybrid under visible light, the final fragments are phenol, pbenzoquinone, malonic acid, butenedioic acid, acetic acid and 25 1,3-butadiene [62].

Combining the studies of other scholars and mass spectrometry analysis, and the molecular structure of the intermediates, one probable degradation pathway of 2,4-DCP could be deduced as shown in Fig. 13.

### 3.8 Photocatalytic Mechanism

On the basis of the above experimental results, a possible photocatalytic mechanism is proposed to explain the enhanced photocatalytic performance, as shown in Fig. 14. The intergrowth and coexistence effects of the mixed-phase TiO<sub>2</sub>-SnO<sub>2</sub>-CuO heterojunctions play a vital role in the enhancement of its photocatalytic activity. The mechanism for the band configuration at the contacted interface of mixed-phase TiO<sub>2</sub>-SnO<sub>2</sub>-CuO material is proposed. Figure 14 shows the schematic diagram of the energy band gap and the charge transfer in the mixed-phase heterojunction system. As we have known, the conduction band (CB) edges of TiO<sub>2</sub> (R), TiO<sub>2</sub> (A), SnO<sub>2</sub> and

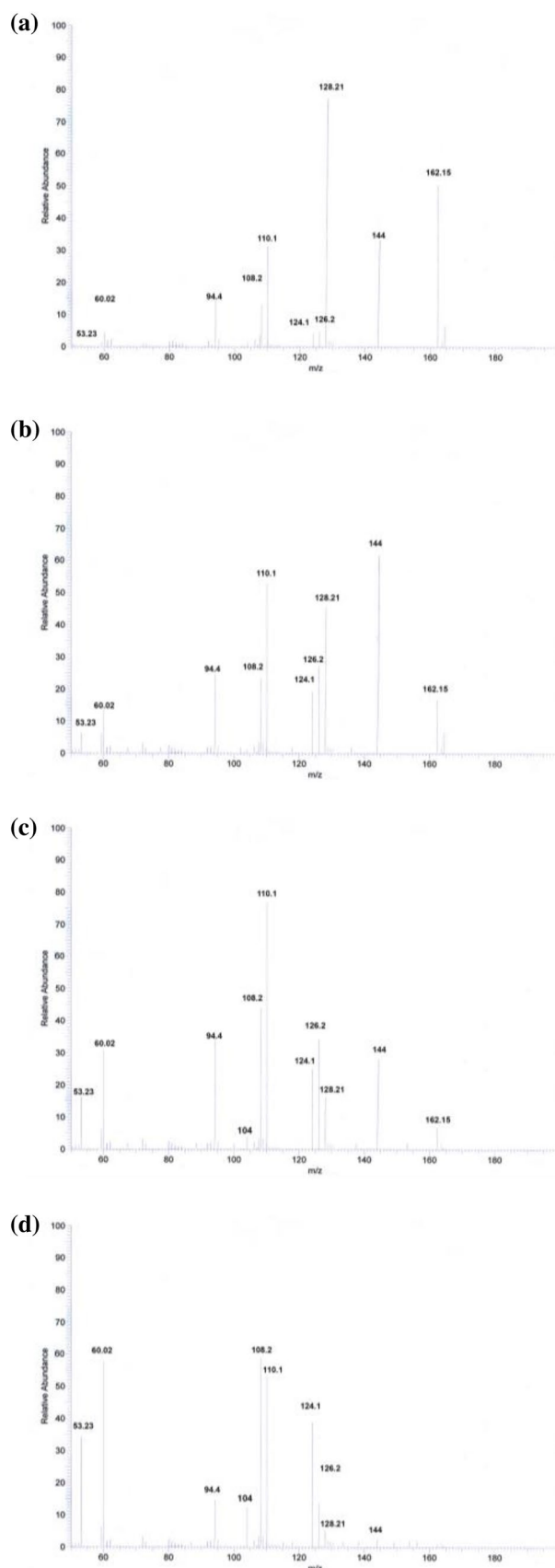


**Table 4** The intermediates identified in the photocatalytic degradation of 2,4 DCP

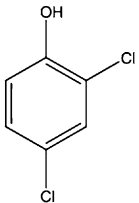
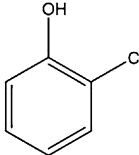
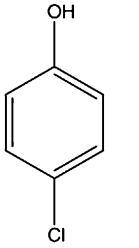
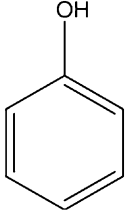
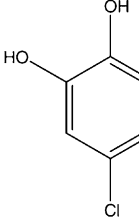
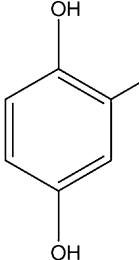
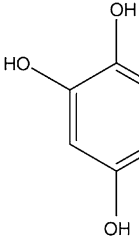
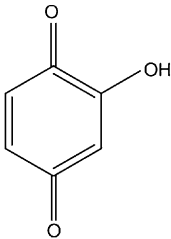
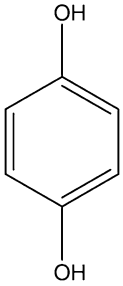
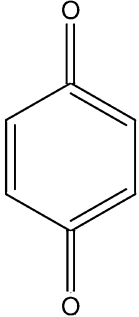
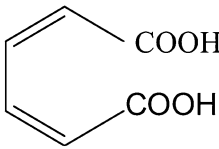
		Molecular ion mass (m/z)	Retention time
	2,4-Dichlorophenol	162.00	4.3
	2-Chlorophenol	128.21	9.32
	4-Chlorophenol	128.21	9.97
			10.1
	4-Chlorohydroquinone	144	7.1
	2-Chlorohydroquinone	144	7.26
	Hydroxyhydroquinone	126.2	4.9



Table 4 (continued)

		Molecular ion mass (m/z)	Retention time
	Hydroxybenzoquinone	124.1	3.04
	Hydroquinone	110.1	11.189
	Benzoquinone	108.09	7.373
		60.02	4.35

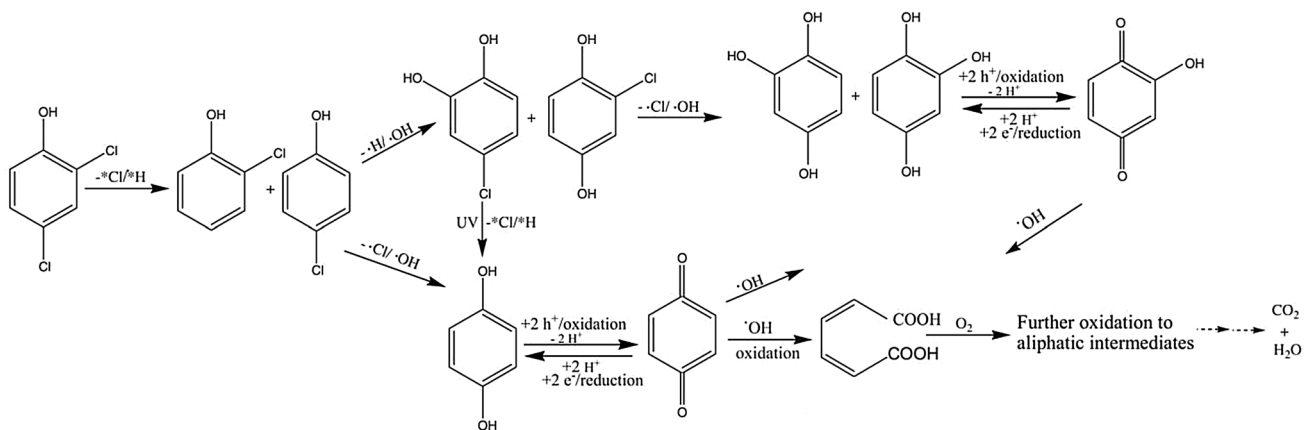
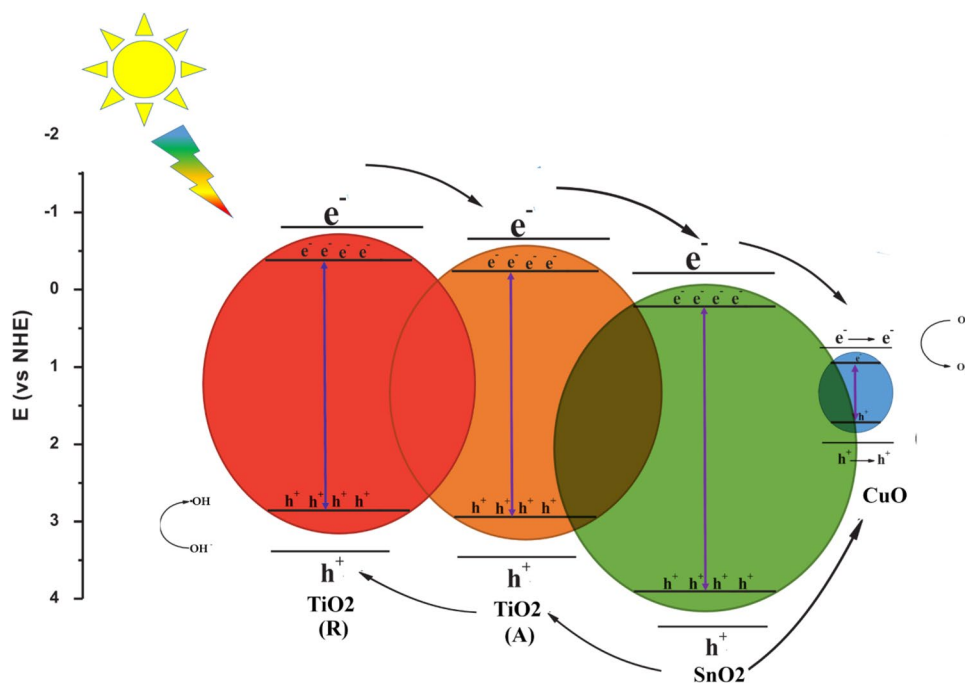


Fig. 13 Possible photocatalytic degradation mechanism of 2,4-DCP by SC10

**Fig. 14** Scheme of photocatalytic mechanism of SnO<sub>2</sub>/CuO/TiO<sub>2</sub>



CuO are  $-0.43$ ,  $-0.21$ ,  $+0.07$  and  $0.27$  eV with respect to normal hydrogen electrode (NHE) while the valence band (VB) edges of TiO<sub>2</sub> (R), TiO<sub>2</sub> (A), SnO<sub>2</sub> and CuO are  $+2.60$ ,  $2.99$ ,  $3.67$  and  $1.6$  eV respectively, suggesting that the system has different electron affinity and band configuration [34, 63, 64]. TiO<sub>2</sub>(A) has the conduction band (CB) edge that is below that of TiO<sub>2</sub> (R) and above that of SnO<sub>2</sub> and CuO [65]. Thus, a ‘staggered’ type II heterojunction at the interface of the mixed-phases is formed. Under light irradiation, electrons in the valence band (VB) of TiO<sub>2</sub> (R) are excited to its CB, while the hole remains in VB, and due to the Fermi energy level of TiO<sub>2</sub> (R) is higher than that of TiO<sub>2</sub>(A), the electrons in CB are driven by the potential energy to transfer to the CB of TiO<sub>2</sub>(A) and then to SnO<sub>2</sub> and CuO. Conversely, the photogenerated hole can move from VB of SnO<sub>2</sub> to that of TiO<sub>2</sub> and CuO [41–43]. It can be seen that in this process the electrons and holes are separated efficiently at the TiO<sub>2</sub>–SnO<sub>2</sub>–CuO interfaces, resulting in a large number of charges could participate in reaction and enhance quantum efficiency. The charge transfer from TiO<sub>2</sub> causes reduction of Ti<sup>3+</sup> ( $\text{Ti}^{3+} - e^- \rightarrow \text{Ti}^{4+}$ ) and the formation of Cu<sup>2+</sup> ( $\text{Cu}^{2+} + e^- \rightarrow \text{Cu}^+$ ). The excess electrons accumulate in CuO, leading to negative shift in Fermi level of CuO. As a result, the Cu<sup>2+</sup> translates into Cu<sup>+</sup> or Cu, which is consistent with the XPS results. Then Cu<sup>+</sup> or Cu gives the excited electrons to oxygen adsorbed on the surface of catalyst. The hole locate in the VB of TiO<sub>2</sub> (R) then reacts with hydroxyl group to produce the hydroxyl radical (OH), which are responsible for photoreaction. On the

basis of the above analysis, we tentatively conclude that combining three semiconductors and two phases with different energy levels to form a ternary hybrid catalyst can facilitate the transfer of the electrons, reduce the recombination probability and increase the charge carrier lifetime, as a consequence of the enhancement of the photocatalytic activity for TiO<sub>2</sub>–SnO<sub>2</sub>–CuO catalysts.

## 4 Conclusion

In summary, a new type of heterostructured photocatalyst by compositing TiO<sub>2</sub> with SnO<sub>2</sub> and CuO is achieved via sol–gel method. Incorporating SnO<sub>2</sub> and CuO into TiO<sub>2</sub> nanoparticles was not improved its photocatalytic performance in UV-light region. On the other hand, under visible light, CuO and SnO<sub>2</sub> addition evidenced the injection of charge-carriers and surely explains the enhanced activity of the composites. Based on the results, it can be concluded that combining three semiconductors with different energy levels to form a ternary hybrid catalyst can facilitate the transfer of the electrons, reduce the recombination probability and increase the charge carrier lifetime, as a consequence of the enhancement of the photocatalytic activity for SnO<sub>2</sub>/CuO/TiO<sub>2</sub> samples. Indeed, enhanced activity was observed for the synthesized SC-0.1 heterojunction, indicating that the recombination of charge carrier is inhibited greatly among all the SnO<sub>2</sub>/CuO/TiO<sub>2</sub> samples.

## References

- Fujishima A, Honda K (1972) Electrochemical photolysis of water at a semiconductor electrode. *Nature* 238:37–38
- Al-Hetlani E, Amin MO, Madkour M (2017) Detachable photocatalysts of anatase TiO<sub>2</sub> nanoparticles: annulling surface charge for immediate photocatalyst separation. *Appl Surf Sci* 411:355–362
- Gu L, Jin C, Wang W, He Y, Yang G, Li G (2017) Transition-metal-free, visible-light induced cyclization of arylsulfonfyl chlorides with o-azidoarylalkynes: a regiospecific route to unsymmetrical 2,3-disubstituted indoles. *Chem Commun* 53:4203–4206
- Park J-H, Ramasamy P, Kim S, Kim YK, Ahilan V, Shanmugam S, Lee J-S (2017) Hybrid metal-Cu<sub>2</sub>S nanostructures as efficient co-catalysts for photocatalytic hydrogen generation. *Chem Commun* 53:3277–3280
- Wu X, Zhao J, Wang L, Han M, Zhang M, Wang H, Huang H, Liu Y, Kang Z (2017) Carbon dots as solid-state electron mediator for BiVO<sub>4</sub>/CDs/CdS Z-scheme photocatalyst working under visible light. *Appl Catal B* 206:501–509
- Hirose Y, Itadani A, Ohkubo T, Hashimoto H, Takad J, Kittaka S, Kuroda Y (2017) Tubular nitrogen-doped TiO<sub>2</sub> samples with efficient photocatalytic properties based on long-lived charge separation under visible-light irradiation: synthesis, characterization and reactivity. *Dalton Trans* 46:4435–4451
- Hu JYR, Meng W, Du Y (2016) A novel p-LaFeO<sub>3</sub>/n-Ag<sub>3</sub>PO<sub>4</sub> heterojunction photocatalyst for phenol degradation under visible light irradiation. *Chem Commun* 52:2620–2623
- Okeil S, Krausmann J, Dönges I, Pflieger S, Engstler J, Schneider JJ (2017) ZnS/ZnO@CNT and ZnS@CNT nanocomposites by gas phase conversion of ZnO@CNT. A systematic study of their photocatalytic properties. *Dalton Trans* 46:5189–5201
- Zhang H, Zhang W, Zhao M, Yang P, Zhu Z (2017) A site-holding effect of TiO<sub>2</sub> surface hydroxyl in the photocatalytic direct synthesis of 1,1-diethoxyethane from ethanol. *Chem Commun* 53:1518–1521
- Lamb R, Umar A, Mehta SK, Kansal SK (2015) ZnO doped SnO<sub>2</sub> nanoparticles heterojunction photo-catalyst for environmental remediation. *J Alloy Compd* 653:327–333
- Reddy CV, Ravikumar RVSSN., Srinivasc G, Shim J, Cho M (2017) Structural, optical, and improved photocatalytic properties of CdS/SnO<sub>2</sub> hybrid photocatalyst nanostructure. *Mater Sci Eng B* 221:63–72
- Pitre SP, Yoon TP, Scaiano JC (2017) Titanium dioxide visible light photocatalysis: surface association enables photocatalysis with visible light irradiation. *Chem Commun* 53:4335–4338
- Lee S-Y, Park S-J (2013) Review: TiO<sub>2</sub> photocatalyst for water treatment applications. *J Ind Eng Chem* 19(6):1761–1769
- Klaysri R, Tubchareon T, Praserttham P (2017) One-step synthesis of amine-functionalized TiO<sub>2</sub> surface for photocatalytic decolorization under visible light irradiation. *J Ind Eng Chem* 45:229–236
- Batalović K, Bundaleski N, Radaković J, Abazović N, Mitrić M, Silva RA, Savić M, Belošević-Čavor J, Rakočević Z (2017) Modification of N-doped TiO<sub>2</sub> photocatalysts using noble metals (Pt, Pd)—a combined XPS and DFT study. *Phys Chem Chem Phys* 19:7062–7071
- Liu G, Yang HG, Pan J, Yang YQ, Lu GQ, Cheng HM (2014) Titanium dioxide crystals with tailored facets. *Chem Rev* 114:9559–9612
- Kim H-i, Kim J, Kim W, Choi W (2011) Enhanced photocatalytic and photoelectrochemical activity in the ternary hybrid of CdS/TiO<sub>2</sub>/WO<sub>3</sub> through the Cascadal electron transfer. *J Phys Chem* 115(19):9797–9805
- Albonetti S, Blasioli S, Bonelli R, Mengou JE, Scirè S, Trifirò F (2008) The role of acidity in the decomposition of 1,2-dichlorobenzene over TiO<sub>2</sub>-based V<sub>2</sub>O<sub>5</sub>/WO<sub>3</sub> catalysts. *Appl Catal A* 341(1–2):18–25
- Kovács G, Baia L, Vulpoi A, Radu T, Karácsonyi É (2014) TiO<sub>2</sub>/WO<sub>3</sub>/Au nanoarchitectures' photocatalytic activity, "from degradation intermediates to catalysts' structural peculiarities", part I: aerioxide P25 based composites. *Appl Catal B* 147:508–517
- Yang G, Yan Z, Xiao T (2012) Preparation and characterization of SnO<sub>2</sub>/ZnO/TiO<sub>2</sub> composite semiconductor with enhanced photocatalytic activity. *Appl Surf Sci* 258:8704–8712
- Nadarajan R, Bakar WAWA., Ali R, Ismail R (2016) Effect of structural defects towards the performance of TiO<sub>2</sub>/SnO<sub>2</sub>/WO<sub>3</sub> photocatalyst in the degradation of 1,2-dichlorobenzene. *J Taiwan Inst Chem Eng* 64:106–115
- Min Z, Wang X, Li Y, Jiang J, Li J, Qian D, Li J (2017) A highly efficient visible-light-responding Cu<sub>2</sub>O–TiO<sub>2</sub>/g-C<sub>3</sub>N<sub>4</sub> photocatalyst for instantaneous discolorations of organic dyes. *Mater Lett* 193:18–21
- Shekofteh-Gohari M, Habibi-Yangjeh A (2016) Fabrication of novel magnetically separable visible-light-driven photocatalysts through photosensitization of Fe<sub>3</sub>O<sub>4</sub>/ZnO with CuWO<sub>4</sub>. *J Ind Eng Chem* 44:174–184
- Liu L, Deng J, Ni T, Zheng G, Zhang P, Jin Y, Jiao Z, Sun X (2017) One-step synthesis of Ag/AgCl/GO composite: a photocatalyst of extraordinary photoactivity and stability. *J Colloid Interface Sci* 493:281–287
- Guerrero-Araque D, Acevedo-Peña P, Ramírez-Ortega D, Calderon HA, Gómez R (2017) Charge transfer processes involved in photocatalytic hydrogen production over CuO/ZrO<sub>2</sub>-TiO<sub>2</sub> materials. *Int J Hydrogen Energy* 42:9744–9953
- Sheng P, Lia W, Du P, Cao K, Cai Q (2016) Multi-functional CuO nanowire/TiO<sub>2</sub> nanotube arrays photoelectrode synthesis, characterization, photocatalysis and SERS applications. *Talanta* 160:537–546
- Luna AL, Valenzuela MA, Colbeau-Justin C, Vázquez P, Rodríguez JL (2016) Photocatalytic degradation of gallic acid over CuO–TiO<sub>2</sub> composites under UV/Vis LEDs irradiation. *Appl Catal A* 521:140–148
- Zhu L, Hong M, Ho GW (2015) Fabrication of wheat grain textured TiO<sub>2</sub>/CuO composite nanofibers for enhanced solar H<sub>2</sub> generation and degradation performance. *Nano Energy* 11:28–37
- Ajmal A, Majeed I, Malik RN, Iqbal M, Nadeem MA, Hussain I, Yousafa S, Zeshan G (2016) Photocatalytic degradation of textile dyes on Cu<sub>2</sub>O–CuO/TiO<sub>2</sub> anatase powders. *J Environ Chem Eng* 4(2):2138–2146
- Wu J, Li C, Chen X, Zhang J, Zhao L, Huang T (2017) Photocatalytic oxidation of gas-phase Hg<sup>0</sup> by carbon spheres supported visible-light-driven CuO–TiO<sub>2</sub>. *J Ind Eng Chem* 46:416–425
- Du F, Zuo X, Yang Q, Yang B, Li G, Ding Z, Wu M, Ma Y, Jin S, Zhu K (2016) Facile assembly of TiO<sub>2</sub> nanospheres/SnO<sub>2</sub> quantum dots composites with excellent photocatalyst activity for the degradation of methyl orange. *Ceram Int* 42(11):12778–12782
- Yuan J, Zhang X, Li H, Wang K, Gao S, Yin Z, Yu H, Zhu X, Xiong Z, Xie Y (2015) TiO<sub>2</sub>/SnO<sub>2</sub> double-shelled hollow spheres-highly efficient photocatalyst for the degradation of rhodamine B. *Catal Commun* 60:129–133
- Huang M, Yu S, Li B, Lihui D, Zhang F, Fan M, Wang L, Yu J, Deng C (2014) Influence of preparation methods on the structure and catalytic performance of SnO<sub>2</sub>-doped TiO<sub>2</sub> photocatalysts. *Ceram Int* 40(8):13305–13312
- Bandara J, Udawatta CPK, Rajapakse CSK (2005) Highly stable CuO incorporated TiO<sub>2</sub> catalyst for photocatalytic hydrogen production from H<sub>2</sub>O Photochem. *Photobiol Sci* 4:857–861
- Moniz SJA, Tang J (2015) Charge transfer and photocatalytic activity in CuO/TiO<sub>2</sub> nanoparticle heterojunctions synthesised through a rapid, One-Pot, Microwave Solvothermal Route. *Chem-CatChem* 7(11):1659–1667

36. Réti B, Péter N, Dombi A, Hernadi K (2013) Preparation of SnO<sub>2</sub>-TiO<sub>2</sub>/MWCNT nanocomposite photocatalysts with different synthesis parameters. *Phys Status solidi* 250(12):2549–2553
37. Zhou B, Yang S, Wu W, Sun L, Lei M, Pan J, Xiong X (2014) Self-assemble SnO<sub>2</sub>@TiO<sub>2</sub> porous nanowire-nanosheet heterostructures for enhanced photocatalytic property. *CrystEngComm* 16:10863–10869
38. Li Y, Hu Z, Liu S, Duan X, Wang B (2014) Comparison of the preparation methods for a highly efficient CuO/TiO<sub>2</sub> photocatalyst for hydrogen generation from water Reaction Kinetics. *Mech Catal* 112(2):559–572
39. Lv X, Wang Y, Lin Z (2016) Study on photocatalytic degradation of 2,4-dichlorophenol by ZnS microsphere. *J Nanosci Nanotechnol* 16(1):1060–1066
40. Kargi F, Eker S (2005) Removal of 2,4-dichlorophenol and toxicity from synthetic wastewater in a rotating perforated tube biofilm reactor. *Process Biochem* 40(6):2105–2111
41. Sinirtas E, Gulim M, Soyul SP (2016) Photocatalytic degradation of 2,4-dichlorophenol with V<sub>2</sub>O<sub>5</sub>-TiO<sub>2</sub> catalysts: effect of catalyst support and surfactant additives. *Chin J Catal* 37(4):607–615
42. Jian Z, Huang S, Zhang Y (2013) Photocatalytic degradation of 2,4-dichlorophenol using nanosized Na<sub>2</sub>Ti<sub>6</sub>O<sub>13</sub>/TiO<sub>2</sub> heterostructure particles. *Int J Photoenergy*. <https://doi.org/10.1155/2013/606291>
43. Rangel-Vázquez I, Angel GD, Bertina V, González F, Vázquez-Zavala A, Arrieta A, Padilla JM, Barrera A (2015) Synthesis and characterization of Sn doped TiO<sub>2</sub> photocatalysts: effect of Sn concentration on the textural properties and on the photocatalytic degradation of 2,4-dichlorophenoxyacetic acid. *J Alloy Compd* 643:144–149
44. Ana H-R, Parka SY, Huh JY, Kim H, Leed Y-C, Lee YB (2017) Nanoporous hydrogenated TiO<sub>2</sub> photocatalysts generated by underwater discharge plasma treatment for solar photocatalytic applications. *Appl Catal B* 15:126–136
45. Yang G, Jiang Z, Shi H, Jones MO, Xiao T (2010) Study on the photocatalysis of F-S co-doped TiO<sub>2</sub> prepared using solvothermal method. *Appl Catal B* 96(3–4):458–465
46. Nguyen DCT, Cho K-Y, Oh W-C (2017) Synthesis of frost-like CuO combined graphene-TiO<sub>2</sub> by self-assembly method and its high photocatalytic performance. *Appl Surf Sci* 412:252–261
47. Renuka L, Anantharaju KS, Vidyad YS, Nagaswarupa HP, Prashantha SC, Sharma SC, Nagabhushana H (2017) A simple combustion method for the synthesis of multi-functional ZrO<sub>2</sub>/CuO nanocomposites: excellent performance as Sunlight photocatalysts and enhanced latent fingerprint detection. *Appl Catal B* 210:97–115
48. Chen J, Liu X, Zhang H, Liu P, Li G, An T, Zhao H (2016) Soft-template assisted synthesis of mesoporous CuO/Cu<sub>2</sub>O composite hollow microspheres as efficient visible-light photocatalyst. *Mater Lett* 182:47–51
49. El-Sheikh SM, Khedr TM, Hakki A, Ismail AA, Badawy WA, Bahnemann DW (2017) Visible light activated carbon and nitrogen co-doped mesoporous TiO<sub>2</sub> as efficient photocatalyst for degradation of ibuprofen. *Sep Purif Technol* 173:258–268
50. Seifvand N, Kowsari E (2017) TiO<sub>2</sub>/in-situ reduced GO/functionalized with an IL-Cr complex as a ternary photocatalyst composite for efficient carbon monoxide deterioration from air. *Appl Catal B* 206:184–193
51. Santhi K, Rani C, Karuppachamy S (2016) Synthesis and characterization of a novel SnO/SnO<sub>2</sub> hybrid photocatalyst. *J Alloy Compd* 662:102–107
52. Hu L, Chen F, Hu P, Zou L, Hu X (2016) Hydrothermal synthesis of SnO<sub>2</sub>/ZnS nanocomposite as a photocatalyst for degradation of Rhodamine B under simulated and natural sunlight. *J Mol Catal A: Chem* 411:203–213
53. Ji X, Liu Y, Wu X, Zhang Z (2014) A low temperature situ precipitation route to designing Zn-doped SnO<sub>2</sub> photocatalyst with enhanced photocatalytic performance. *Appl Surf Sci* 311:609–613
54. Kuang Q, Wang X, Jiang Z, Z ZX, and Zheng L (2014) High-energy-surface engineered metal oxide micro- and nanocrystallites and their applications. *Acc Chem Res* 47(2):308–318
55. Lu Q, Yu J, Gao J (2006) Degradation of 2,4-dichlorophenol by using glow discharge electrolysis. *J Hazard Mater* 136(3):526–531
56. Wang Y, Shen Z, Li Y, Niu J (2010) Electrochemical properties of the erbium-chitosan-fluorine-modified PbO<sub>2</sub> electrode for the degradation of 2,4-dichlorophenol in aqueous solution. *Chemosphere* 79:987–996
57. Liu L, Chen F, Yang F (2009) Stable photocatalytic activity of immobilized Fe<sub>0</sub>/TiO<sub>2</sub>/ACF on composite membrane in degradation of 2,4-dichlorophenol. *Sep Purif Technol* 70(2):173–178
58. Xu LJ, Wang JL (2012) Fenton-like degradation of 2, 4-dichlorophenol using Fe<sub>3</sub>O<sub>4</sub> magnetic nanoparticles. *Appl Catal B* 123–124:117–126
59. Zhang J, Liu D, Bian W, Chen X (2012) Degradation of 2,4-dichlorophenol by pulsed high voltage discharge in water. *Desalination* 304:49–56
60. Chung S-G, Chang Y-S, Choi J-W, Baek K-Y, Hong S-W, Yun S-T, Lee S-H (2013) Photocatalytic degradation of chlorophenols using star block copolymers: removal efficiency, by-products and toxicity of catalyst. *Chem Eng J* 215–216:921–928
61. Devi LG, Nithya PM (2018) Photocatalytic activity of Hemin (Fe(III) porphyrin) anchored BaTiO<sub>3</sub> under the illumination of visible light: synergetic effects of photosensitization, photo-Fenton & photocatalysis processes. *Inorg Chem Front* 5:127–138
62. Rakibuddina M, Ananthakrishnan R (2016) Effective photocatalytic dechlorination of 2,4-dichlorophenol by a novel graphene encapsulated ZnO/Co<sub>3</sub>O<sub>4</sub> core-shell hybrid under visible light. *Photochem Photobiol Sci* 15:86–98
63. Marschall R (2014) Semiconductor composites: strategies for enhancing charge carrier separation to improve photocatalytic activity. *Adv Funct Mater* 24:2421–2440
64. Scanlon D, Dunnill CW, Buckeridge J, Shevlin SA, Logsdail AJ, Woodley SM, Catlow CR, Powell MJ, Palgrave RG (2013) Band alignment of rutile and anatase TiO<sub>2</sub>. *Nat Mater* 12(9):798–801
65. Kumar A, Rout L, Achary LSK, Mohanty A, Marpally J, Chand PK, Dash P, (2016) Design of binary SnO<sub>2</sub>-CuO nanocomposite for efficient photocatalytic degradation of malachite green dye. In: *AIP Conference Proceedings* 1724